

## Full Length Article

# Dense and hard TiWC protective coatings grown with tungsten ion irradiation using WC-HiPIMS/TiC-DCMS co-sputtering technique without external heating

Tun-Wei Hsu<sup>a,\*</sup>, Grzegorz Greczynski<sup>b</sup>, Robert Boyd<sup>a</sup>, Szilárd Kolozsvári<sup>c</sup>, Peter Polcik<sup>c</sup>, Magnus Odén<sup>a</sup>

<sup>a</sup> Nanostructured Materials Division, Department of Physics (IFM), Linköping University, SE-58183 Linköping, Sweden

<sup>b</sup> Thin Film Physics Division, Department of Physics (IFM), Linköping University, SE-58183 Linköping, Sweden

<sup>c</sup> Plansee Composite Materials GmbH, Lechbruck am See, DE-86983, Germany

## A B S T R A C T

Titanium tungsten carbide (TiWC) coatings are deposited by a combined high-power impulse and dc magnetron co-sputtering (HiPIMS/DCMS) technique. No external heating is applied during deposition phase, instead, the thermally driven adatom mobility is substituted by heavy ion irradiation. DCMS sources equipped with titanium carbide targets provide constant neutral fluxes to establish the predominant coating structures, whereas tungsten carbide target in HiPIMS mode serves as the source of heavy metal-ions. Substrate bias of  $-60$  V is synchronized to  $W^+$  ion-rich time domains of HiPIMS pulses to minimize the contribution from working gas ions. The influence of  $W^+$  ion flux intensity, controlled by varying peak target current density ( $J_T$ ), on film properties is investigated. X-ray photoelectron spectroscopy reveals the presence of over stoichiometric carbon forming an amorphous phase, the amount of which can be fine-tuned by varying  $J_T$ . Changes in film composition as a function of  $J_T$  are explained based on the in-situ ion mass spectroscopy analyses. Dense TiWC coatings by hybrid process exhibit hardness higher than 30 GPa, which are comparable to TiWC films deposited by DCMS with dc substrate bias and external heating. The relative energy consumption in the hybrid process is reduced by 77 % as compared to high-temperature DCMS processing.

## 1. Introduction

Protective layers applied on metal machining tool surfaces are proven to be an effective approach to improve their performance and lifetime. Typically, the operating conditions of the tool surface is harsh, with high temperatures and pressures. Transition metal nitrides and carbides are common materials for such applications, due to their high strength and durability [1]. Titanium carbide (TiC) is frequently used to coat metal machining tools because of its good intrinsic properties [2]. The properties of deposited TiC depend on the carbon content. Excess carbon may form an amorphous phase (a-C), which encapsulates the crystalline TiC nanograins to form a nc-TiC/a-C(:H) nanocomposite. For a specific amount of this a-C tissue phase, super hardness ( $H \geq 40$  GPa) has been observed [3,4]. Growth of TiC coatings is typically achieved by chemical vapor depositions (CVD) [5,6] and physical vapor depositions (PVD) [7–9] techniques.

Various approaches have been applied to further improve the performance of the TiC-based material system. One promising route is to introduce an additional element to form ternary carbides. Edström et al.

[10] have theoretically shown for TiMeC (Me = tungsten (W) or molybdenum (Mo)), that their relative hardness enhancement compared to TiC is related to the introduction W-C and Mo-C bonds, with more covalent character, to the strongly ionic-bonded TiC. Hardness enhancements from alloying TiC with other metal elements have also been observed experimentally. For example, Ji et al. [11] attributed the hardness enhancement of CVD prepared Ti-W-C to the formation of additional WC phases. Koutzaki et al. [12] observed comparable hardness of sputtered Ti-W-C and TiC coatings, while specific nanocomposite Ti-W-C microstructures displayed higher hardness due to Hall-Petch strengthening.

Another approach to improve the mechanical properties of coatings is to apply energetic particle bombardment during depositions by applying a negative bias voltage to the substrate to attract and accelerate positive ions toward the growing film surface, e.g., metal ions in cathodic arc deposition [13] or Ar-ions in magnetron sputtering [9]. The increased adatom mobility caused by the ion irradiation in combination with any external substrate heating facilitate growth of dense and hard coatings. Potential drawback with this approach is the generation of

\* Corresponding author.

E-mail address: [tun-wei.hsu@liu.se](mailto:tun-wei.hsu@liu.se) (T.-W. Hsu).

<https://doi.org/10.1016/j.apsusc.2023.156639>

Received 21 December 2022; Received in revised form 23 January 2023; Accepted 31 January 2023

Available online 2 February 2023

0169-4332/© 2023 The Author(s). Published by Elsevier B.V. This is an open access article under the CC BY license (<http://creativecommons.org/licenses/by/4.0/>).

high compressive stresses that promotes cohesive failure of the coating and adhesive failure at the substrate-coating interface [14], and entrapment of impurities such as species from the working gas used in magnetron sputtering [15]. In addition, the energy consumption is high, as in addition to the substrates, also the entire vacuum chamber is heated up. Another drawback is the limited selection of suitable substrate materials that can tolerate high temperatures.

Recently, a novel hybrid high-power impulse and dc magnetron co-sputtering (HiPIMS/DCMS) technique with metal-ion-synchronized substrate bias was introduced to overcome these drawbacks [16]. Here, HiPIMS serves as a source of metal-ions during short regular pulses [17], which arrive at the substrate out-of-phase with respect to the arrival of gas ions [18]. Synchronizing substrate bias pulses with the HiPIMS pulses and correctly setting the time delay and the duration of the bias pulses gives control over the energy and momentum transfer of metal-ions to the growing coating [19]. Tuning the time delay such that working gas ions arrive at the coating growth front when the substrate is electrically floating results in low energy and momentum transfer, which is insufficient to cause ion implantation and lattice distortion. Hence, working gas incorporation and high compressive stresses can be avoided. The continuous flux of neutrals from the DCMS source allows for high deposition rate from the HiPIMS/DCMS co-sputtering setup, while the metal ions supplied by the HiPIMS source are accelerated by the synchronized substrate bias and effectively densify the growing film, provided that the incident ion mass is sufficiently high [20,21]. The ion irradiation is even effective enough to render sufficient adatom mobility to deposit dense and hard coatings without external heating. For example, Li et al. [22] recently demonstrated the relationship between coating densification and the mass of the metal ion by using a Me-HiPIMS/TiAl-DCMS setup (Me = Cr, Mo, or W). Their results show that W-ion irradiation most effectively densified the coatings compared with the lighter metal ions. Coatings grown with W-ion radiation and without external heating had a hardness of 32 GPa, which is similar to  $\text{Ti}_{0.5}\text{Al}_{0.5}\text{N}$  coatings grown at 500°C, while the energy consumption was reduced by 83 %. Similar approach has also been applied for growth of other transition metal nitrides [23–25], while it is yet to be evaluated for transition metal carbides.

Another aspect is that to deposit carbides typically reactive physical vapor deposition (PVD) processes employing, e.g., acetylene ( $\text{C}_2\text{H}_2$ ), are used. This implies health hazards and has a negative impact on the environment [26]. Both issues can be resolved by using compound carbide targets provided that the process flexibility allows for control of the carbon content in the films, which determines mechanical properties.

In this study, we use high-mass  $\text{W}^+$  irradiation to evaluate densification effects during growth of TiWC coatings by WC-HiPIMS/TiC-DCMS with synchronized substrate bias. The growth is performed from compound targets, thus avoiding acetylene, and with no substrate heating (to reduce energy consumption). By controlling the peak target current density at the HiPIMS source to alter the intensity of  $\text{W}^+$  ion fluxes, we demonstrate the enhancement of the mechanical properties and the possibility to fine tune a-C content in the films.

## 2. Experimental details

### 2.1. Film deposition

The depositions were performed in the CemeCon AG CC800/9 deposition system, in which three sources were operated simultaneously and the Si (100) substrates were positioned 18.5 cm away from the HiPIMS target surface. A thermocouple mounted close to substrate position was used to record the deposition temperature. The substrates,  $1.0 \times 2.0 \text{ cm}^2$  were cleaned in a mixture of acetone and isopropanol using an ultrasonic bath and blow-dried with  $\text{N}_2$  gas prior to being inserted into the deposition chamber. The source arrangement with

respect to the substrate position is illustrated in Fig. 1.

The source operated in HiPIMS mode is positioned in between the two cathodes operated in DCMS mode.  $\text{Ti}_{0.5}\text{C}_{0.5}$  targets were mounted on the DCMS sources, while a  $\text{W}_{0.5}\text{C}_{0.5}$  target was mounted on the HiPIMS source. All targets have the same dimension,  $8.8 \times 50 \text{ cm}^2$ .

The deposition parameters are summarized in Table 1. To establish the influence of W ion irradiation, reference TiWC films were deposited by operating the  $\text{W}_{0.5}\text{C}_{0.5}$  target in DCMS mode. The reference films are used for comparison with films grown with the DCMS/HiPIMS hybrid configuration. To maintain similar tungsten to titanium elemental ratio of the reference coatings as the W-ion radiated films, the WC target was operated with different power settings ranging from 220 to 260 W. The power of each DCMS source equipped with TiC targets was kept constant at 4500 W.

For films grown with W-ion radiation using the HiPIMS/DCMS hybrid configuration, the HiPIMS power and frequency were kept constant at 500 W with 100 Hz, respectively. Different pulse lengths were used (20, 30, 40, 50, 100, and 200  $\mu\text{s}$ ) since it is the primary parameter controlling the peak target current densities ( $J_T$ ) at constant average power and frequency [27]. The HiPIMS waveforms are shown in Fig. 2. The resulting  $J_T$  varies from 0.27 to  $1.36 \text{ A/cm}^2$ . The entire surface area of the target was used to estimate the current densities and the obtained values should be interpreted as lower limits. The current density is a rough measure of the W ionization since the ionization mechanism in HiPIMS is mainly electron impact ionization, thus the ionization efficiency of the sputter-ejected atoms increases with increasing the plasma density that increases with  $J_T$  [28]. The DCMS power was adjusted between 2150 and 4500 W to keep the elemental ratio similar between all samples.

The pulsed substrate bias of  $-60 \text{ V}$  was synchronized to the HiPIMS pulses. The substrate bias pulse was delayed by 30  $\mu\text{s}$  with respect to the ignition of the HiPIMS pulse and its 200  $\mu\text{s}$  duration captured the metal ion rich portion of the HiPIMS pulse. The pulse offset and duration values were selected based on the time resolved analyses of  $\text{W}^+$  ion fluxes impinging at the substrate reported elsewhere using the same deposition chamber [24] but a W target operated in HiPIMS mode in 0.4 Pa Ar/ $\text{N}_2$  atmosphere with a peak current density of  $0.5 \text{ A/cm}^2$ .

Proper outgassing of the deposition system was ensured by a one-hour-long heating cycle, during which a maximum temperature of 250 °C was reached. After that, the system was allowed to cool down for an hour, which resulted in a background pressure of less than 0.75 mPa.

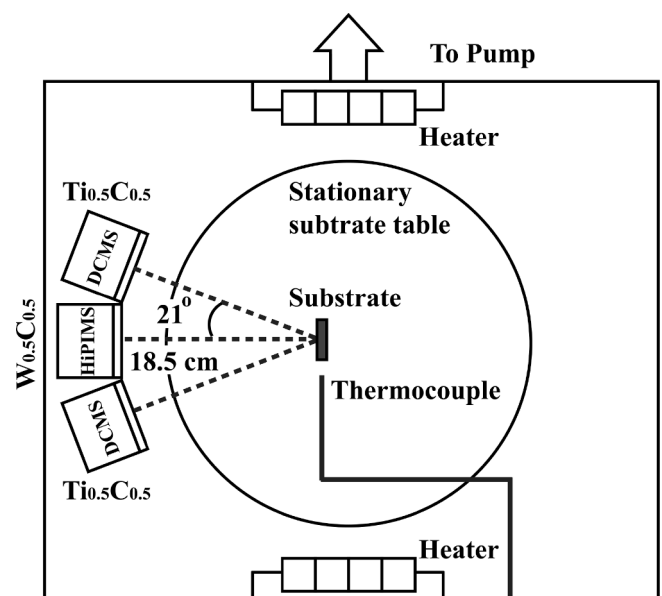
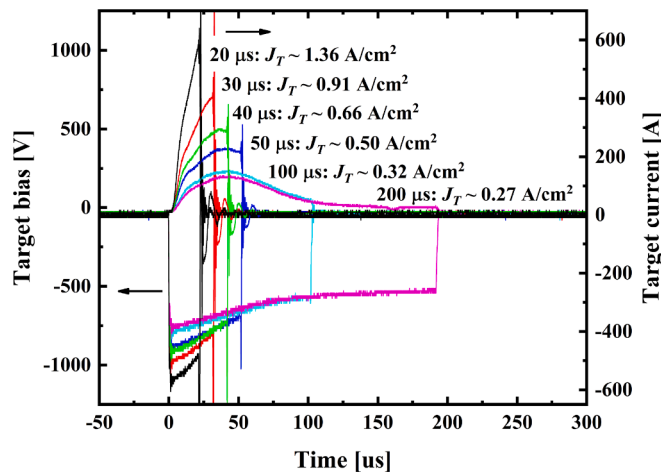


Fig. 1. Schematic illustrations of CemeCon CC800 system with the target-to-substrate configuration.

**Table 1**

Deposition parameters used for the growth of TiWC and TiC samples.

Single DC	HiPIMS			Heating	Bias
Power (W)	Pulse length ( $\mu$ s)	Peak current (A)	Power /Frequency	Power, Temperature	Bias/Pulse length
2150	20	600	500 W/100 Hz	No (<180 °C)	-60 V/ 200 $\mu$ s (30 $\mu$ s offset)
2700	30	400			
3180	40	290			
3200	50	220			
3900	100	140			
4500	200	120			
4500	DC	–	300 W	Yes (<470 °C)	Self-biasing -60 V/ DC Self-biasing -60 V/ DC
4500			300 W		
4500			220 W		
4500			260 W		
4000		–		No (<180 °C)	Self-biasing

**Fig. 2.** Target bias (V) and current (A) waveforms recorded during the WC-HiPIMS/TiC-DCMS deposition with the pulse length variations from 20 to 200  $\mu$ s. Peak target current densities,  $J_T$ , were calculated by taking the entire target surface.

After cooling, the substrate temperature, measured by a calibrated thermocouple, were lower than 140 °C prior to the depositions. During the deposition, no external heating was applied to the substrate. Due to the plasma heating, the deposition temperatures increased but did not exceed 180 °C. For DCMS configuration with heating, the system went through a two-hour heating phase with heaters powered to 8.8 kW to reach the deposition temperature of 480 °C. During the deposition, both heaters were powered to 8 kW. The total pressure was 0.39 Pa with Ar gas during all depositions. Deposition times varied in between 30 and 55 min to achieve film thicknesses of  $1.8 \pm 0.1 \mu\text{m}$  ( $1.5 \mu\text{m}$  for DCMS configuration films).

## 2.2. Characterization techniques

Film thickness and morphology were observed by a LEO 1550 scanning electron microscope (SEM) using an acceleration voltage of 5 kV and a working distance of 5 mm. The plan-view transmission electron microscopy (TEM) images were acquired by Fei Tecnai G<sup>2</sup> TF 20 UT operated with an acceleration voltage of 200 kV. The electron transparent plan view samples were prepared by focus ion beam (FIB) milling of wedge shaped specimens using a dual beam system (Zeiss 1540

crossbeam, Zeiss). Quantitative elemental compositions were determined by time-of-flight elastic recoil detection analysis (ToF-ERDA) using a 36 MeV  $^{127}\text{I}^{8+}$  probe beam at 67.5° incidence angle with recoils detected at 45°.

X-ray diffractometry (XRD) was performed with a Philips X'Pert MRD system in Bragg–Brentano configuration and using a point-focus Cu-K $\alpha$  radiation ( $\lambda = 0.154 \text{ nm}$ ) source. To resolve the wurtzite peaks overlapping with the forbidden 200Si-substrate peak [29] and overcome crystallographic texture effects, a series of  $\theta$ -2 $\theta$  diffractograms were recorded at different tilts ( $\psi$ ) of the sample, i.e., the angle between the substrate surface normal and the diffraction vector was varied between 0 and 71.6°. The residual stress in the multiphase films was determined by the curvature method by recording the curvature of the single crystal substrate through a series of rocking curve measurements [30]. The rocking curve measurements of Si (400) reflection were carried out at 9 equally spaced points along a straight line on each sample using a PANalytical Empyrean diffractometer equipped with an X-ray lens and a 3-bounce Ge (200) monochromators as primary and secondary optics, respectively. The stress in the film was then calculated by the Stoney equation [31] and using the modulus of Si (001),  $E_s/(1-\nu_s) = 181 \text{ GPa}$ , at room temperature [32].

X-ray photoelectron spectroscopy (XPS) core-level spectra were acquired with a Kratos Axis Ultra DLD instrument with a base pressure lower than  $1.5 \times 10^{-7} \text{ Pa}$ . Monochromatic Al-K $\alpha$  radiation ( $h\nu = 1486.6 \text{ eV}$ ) was used while the electron emission was recorded along the surface normal. To remove surface contaminants, Ar<sup>+</sup> ion etching was used. First, 4 keV Ar<sup>+</sup> ions incident at a 70° angle from the surface normal were employed for 2 min. After that the surface was further etched with 0.5 keV Ar<sup>+</sup> ions for additional 10 min to minimize beam damage effects on core-level spectra [24,33]. All spectra were charge-referenced to the Fermi edge cut-off (see Fig. S1), which is a more reliable approach than the C 1s method [34]. Due to wide spread of reported binding energy (BE) values for the W 4f<sub>7/2</sub> peak of WC ( $\Delta_{BE} \approx 0.8 \text{ eV}$  [35]), we acquired reference spectra from the WC-Co substrate, in which the WC-phase has a hexagonal crystal structure (h-WC, c.f., Fig. S2). The 6 wt% Co added as a binder does not affect and the W 4f and C 1s peaks that appear at 282.9 and 31.7 eV, respectively (c.f., Fig. S4-5). The spectra were analyzed by CasaXPS software using Shirley background and Gaussian and Lorentzian line shapes.

The ion mass spectrometry analyses were performed using an EQP 9 mass-energy analyzer (MEA) from Hiden Analytical. The data was measured at the substrate plane and under the same conditions as during film growth. The time-averaged mass/charge (m/q) scans were recorded from 2 to 200 amu with the step of 0.2 amu and for the ion energy of 10 eV. The time-resolved ion fluxes were recorded with the 10  $\mu$ s resolution covering the time period from 0 to 230  $\mu$ s after the ignition of the HiPIMS pulse. The data for calculating ion flux ratios were recorded during 100 consecutive HiPIMS pulses, which gives a total acquisition time of 1 ms per data point. The results were corrected for the mass-dependent ion time-of-flight (TOF) from the orifice to the detector, according to procedures described in Ref. [36]. The ion energy,  $E_i$ , was scanned from  $E_i = 1$  to 50 eV for most ions with a step size of 1 eV, except 0 to 30 eV for Ar<sup>+</sup>. Correspondingly, the data were treated with corrections to compensate abundance of isotopes, ion charges, and mass. For isotope correction, the measured intensity was divided by the natural abundance of the selected isotope [37]. The abundance numbers are 8.25 %, 33.6 %, 1.07 %, and 30.64 % for the selected isotopes  $^{46}\text{Ti}^+$ ,  $^{36}\text{Ar}^+$ ,  $^{13}\text{C}^+$ , and both  $^{184}\text{W}^+$  and  $^{184}\text{W}^{2+}$  [38]. For charge correction, the data of doubly charged  $\text{W}^{2+}$  were corrected by multiplying the ion energy and dividing the intensity by a factor of two [39]. For mass correction, intensities were corrected for the 1/mass instrument transmission function according to vendor recommendations.

An UMIS nanoindenter equipped with Berkovich diamond tip was used to measure the hardness, H. Depth sensing indentations were performed with a maximum load of 15 mN, which yielded indentation depths <10 % of the film thicknesses. The hardness was extracted from

the unloading curves using the Oliver and Pharr method [40]. A minimum of 25 indents were used to determine the reported average hardness values.

### 3. Results and discussion

#### 3.1. Elemental composition

The elemental composition measured by ERDA is presented in Fig. 3. All TiWC samples are over stoichiometric in carbon,  $51.6 \pm 0.8 \leq [\text{C}] \leq 55.8 \pm 0.8$  at%. The TiWC samples grown by DCMS have higher carbon contents than the ones grown by the hybrid technique. The carbon content increases with decreasing  $J_T$  (x-axis, where DC has the lowest  $J_T$ ). Samples without W, i.e., TiC, have the highest carbon content,  $[\text{C}] = 56.8 \pm 0.6$  at%. The metal fractions are similar for all TiWC samples,  $0.11 \leq [\text{W}]/([\text{W}] + [\text{Ti}]) \leq 0.14$ , but most of the samples are  $0.12 \sim 0.13$ . Oxygen content is below 1 at% for the samples grown with substrate bias. In contrast, higher [O] are detected in samples grown at the floating potential. DCMS mode TiWC samples have  $[\text{O}] \approx 2 \pm 0.2$  at% and TiC samples have  $[\text{O}] = 4.4 \pm 0.1$  at%. Other detected elements, [Ar] and [N], are both below 1 at% for all samples.

#### 3.2. Crystal phase analysis

X-ray  $\theta$ - $2\theta$  diffractograms of TiWC films are presented in Fig. 4. To detect the presence of textured phases that are oriented such that low indices planes are not parallel to the sample surface and to suppress the signal of the substrate, the  $\theta$ - $2\theta$  diffractograms were recorded at different sample tilt angles,  $\psi$ . The peak around  $2\theta = 32.98^\circ$  at  $\psi = 0^\circ$  is the forbidden Si 200 reflection from the single-crystal Si substrate [29]. For all TiWC samples, there is no indication of the hexagonal WC structure. The peaks around  $2\theta = 35.4^\circ$  and  $41.1^\circ$  correspond to the 111 and 200 reflections from B1 structured TiWC solid solution. In comparison to the c-TiC reference (PDF: 00-032-1383 [41]), both peaks shift toward lower  $2\theta$  angles, which is the result of residual stress and incorporation of W into c-TiC. All samples are crystalline with preferred 111 orientation. The 111 and 200 peak intensity ratio,  $I_{111}/(I_{111} + I_{200})$ , at  $\psi = 0^\circ$  continuously decreases from 0.96 to 0.73 with increasing  $J_T$ . The transition towards a stronger 200 component of the texture is an effect of enhanced adatom mobilities at, or near the surface region when the ion irradiation increases. Such evolutions were previously reported

for B1 structured TiAlN [42] and TiN [43]. Similar to TiN, the (002) surfaces have lower energy than (111) surfaces in stoichiometric TiC [44]. With increasing number of  $\text{W}^+$  ions, the energy gained from the potential drop of  $-60$  V and the energy transfer, by collisions, between  $\text{W}^+$  ions and Ti atoms at the surface provides enough adatom mobilities to form more thermodynamically favorable (002)-oriented grains. In contrast, growth under more energy limited conditions such as DCMS where the ion irradiation is dominated by low mass  $\text{Ar}^+$  ions, provide less adatom mobility that results in the growth of the close packed (111) surface. In addition, for B1 structure, the [100] directions are the most open ones resulting in less resputtering because a larger fraction of the incoming ions are being channeled into the film and lose their energy over larger distances. Due to this selection mechanism, (002) planes have higher probability to survive ion irradiation [45].

#### 3.3. Chemical bonding characteristics

Fig. 5 shows XPS spectra of C 1s, Ti 2p, and Ti 3p/W 4f regions for the WC-HiPIMS/TiC-DCMS TiWC film grown with  $J_T = 1.36 \text{ A/cm}^2$  and the TiC DCMS self-biased sample. All the other specimens display similar spectra in terms of peak profiles and positions and a complete data set can be found in the supplementary material, Figs. S3-S5. For both TiC (Fig. 5 (a)) and TiWC (Fig. 5 (b)), Ti 2p spectra consist of the spin-orbit-split doublet with  $2p_{3/2}$  and  $2p_{1/2}$  components at 454.9 and 460.9 eV, respectively. Similar BE of Ti 2p ( $2p_{3/2} \sim 454.7$  eV and  $2p_{1/2} \sim 460.8$  eV) have previously been reported for TiC [33].

Fig. 5 (d) shows the W 4f spectrum of the TiWC film. It exhibits three peaks at 32.1, 34.3, and 37.8 eV assigned to  $\text{W } 4f_{7/2}$ ,  $\text{W } 4f_{5/2}$ , and  $\text{W } 5p_{3/2}$ , respectively. The primary  $\text{W } 4f_{7/2}$  peak position at 32.1 eV is shifted toward higher BE by  $\Delta_{BE} \approx 0.4$  eV with respect to the  $\text{W } 4f_{7/2}$  peak recorded from our WC-Co reference (31.7 eV). The  $4f_{7/2}$ -to- $4f_{5/2}$  peak area ratio does not agree with the theoretical value of 4:3 based on the degeneracy of the spin states [46]. This is caused by an overlap with the Ti 3p signal that appears in the same BE range, around 33.8 eV, as clearly shown for the TiC sample in Fig. 5 (c), which means that it predominantly overlaps with the  $\text{W } 4f_{5/2}$  component in the W 4f spectra from TiWC (see Fig. 5 (d)).

The C 1s spectrum of the TiC sample is shown in Fig. 5 (e). Three distinct components are resolved by performing peak fitting. The spectrum consists of a C-Ti peak at 281.8 eV, a C—C peak at 284.5 eV, and an additional peak denoted as C-Ti\* at 282.8 eV. The C—C component is associated with the presence of a-C phases [47]. Its BE, 284.5 eV, is in the frequently reported range, 284.1 to 284.9 eV, of C—C components [48]. The C-Ti peak originates from C incorporated in the TiC grains [33]. Lewin et al. [47] suggested the C-Ti\* peak to originate from the a: C/n-TiC interface. Our TiC contains 56.8 at% (c.f., Fig. 3), hence, the observation of the C-Ti\* peak is expected due to the presence of over-stoichiometric carbon. However, the other structures caused by  $\text{Ar}^+$  sputter damage may also contribute to the C-Ti\* peak [49]. The symmetric line shape was used to represent the C—C peak, whereas the asymmetric line shape was employed for C-Ti due to its metallic nature. The exact parameters of asymmetric line shapes were determined by fitting stoichiometric TiC (i.e., without a-C phase) reference sample previously analyzed in the same instrument and under the same measurement conditions [33]. The same asymmetric line shape was employed to represent the C-Ti\* component in all C 1s spectra.

Input from the fitted C 1s spectrum of the reference TiC was used to peak fit the more complex C 1s spectrum acquired from the sputter-etched TiWC film grown with  $J_T = 1.36 \text{ A/cm}^2$ . The C-Ti\* component is also included in the fitting analysis. The fitted C 1s spectrum is presented in Fig. 5 (f), which comprises C-Ti (282.0 eV), C-W (282.5 eV), C-Ti\* (283.0 eV), and C—C (284.4 eV) components. The chemical shift,  $\Delta_{BE} \approx 1$  eV, between C-Ti and C-Ti\* was constrained based on the fitting of the C 1s spectrum of TiC (c.f., Fig. 5 (e)). The C-W component is fitted with the same asymmetric line shape as used for the C-Ti peak. The peak ratio between C-W and C-Ti components was constrained to the value

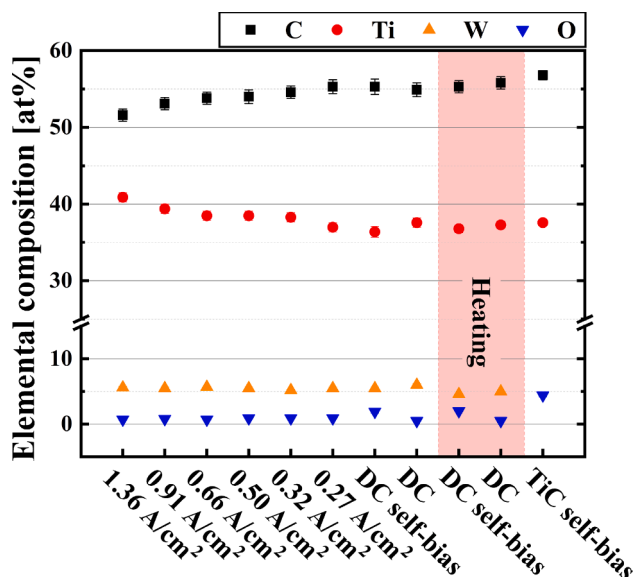


Fig. 3. Elemental composition measured by ERDA. To show the trend better, a break from 15 to 25 at% is given.



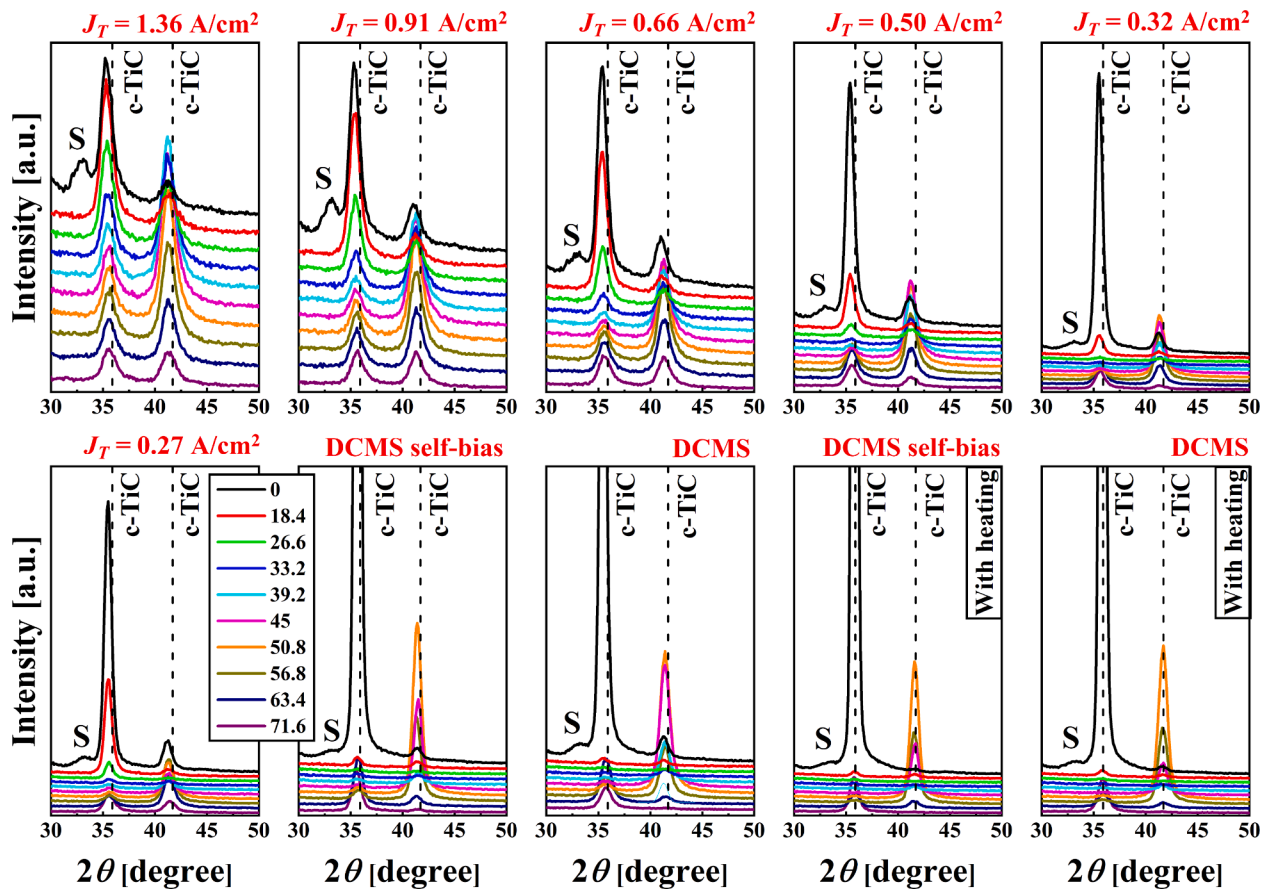


Fig. 4. X-ray  $\theta$ - $2\theta$  diffractograms from  $30^\circ$  to  $50^\circ$  with tilt angles from  $0^\circ$  to  $71.6^\circ$  of TiWC samples grown by hybrid co-sputtering without external heating to DCMS growth without and with external heating. S indicates the substrate signal from Si at  $\psi = 0^\circ$ .

determined by the sample stoichiometry as evaluated from the XPS survey spectrum (to account for possible preferential sputtering during  $\text{Ar}^+$  etching). The C-W peak at 282.5 eV is shifted toward lower BE by  $\sim 1$  eV in comparison to the values reported for  $\text{W}_2\text{C}$  (283.45 eV [33]) and by  $\sim 0.4$  eV compared to our WC-Co reference (282.9 eV). This is because the reference WC has a hexagonal crystal structure, while films in this study has the B1 cubic structure, i.e., from W atoms in the c-TiWC solid solution (c.f., Fig. 4). Consequently, different valence charge distribution is expected. Peak shifts suggest that valence charge density is higher on C atoms in solid solution c-TiWC than in the hexagonal WC structure. The opposite is true for W atoms.

### 3.4. The origin of carbon over-stoichiometry

The carbon content determined by ERDA (Fig. 3) and the C 1s signal fraction corresponding to the C—C peak are plotted for all films in Fig. 6. Differences between bulk-probing ERDA data and the surface-sensitive XPS technique are expected. In particular, the destructive  $\text{Ar}^+$  etching process applied before XPS measurements to remove the contaminants alters the surface composition [49,50]. Nevertheless, both ERDA and XPS results are in agreement: while the carbon content estimated from ERDA continuously decreases with increasing  $J_T$  (x-axis, where DCMS has the lowest  $J_T$ ), the fraction of C—C bonds (corresponding to amorphous C) also goes down. The highest value is obtained for the TiC sample.

A higher carbon-to-metal ratio in the films than in the targets have also been observed during DCMS from  $\text{Ti}_3\text{SiC}_2$  [51,52] and  $\text{Ti}_2\text{AlC}$  [53] compound targets. Films enriched in the lighter component have also been reported for other compound targets than carbides. For example, using titanium-boron (Ti-B) compound target, Neidhardt et al. [54]

suggested that the Ti deficiency in the films is due to two factors: differences in the Ti and B emission characteristics from the  $\text{TiB}_2$  target and scattering processes in the plasma. Considering the atomic masses of the target constituents ( $m_B = 10.8$ ;  $m_{\text{Ti}} = 47.9$  amu [38]) in relation to that of impinging gas ions ( $m_{\text{Ar}} = 39.9$  amu [38]), lighter B experiences fewer collisions than Ti before leaving the target surface. Thus, B flux is preferentially emitted along the target normal, while Ti emission is close to the cosine distribution. Additionally, due to the differences in covalent radii ( $r_B = 87$ ;  $r_{\text{Ti}} = 176$  pm [55]) sputter-ejected Ti and B atoms scatter differently during gas phase transportation with smaller and lighter B atoms having longer mean free paths. As a result of the above effects,  $\text{TiB}_x$  films deposited under low gas pressure and with the substrates placed along the target normal and closer to target are Ti deficient.

The above arguments can also be used to explain the apparent C over stoichiometry in TiWC films sputtered from compound targets as also in this case there is a large difference between target constituents in both covalent radii ( $r_C = 67$ ;  $r_{\text{Ti}} = 176$ ;  $r_W = 193$  pm [55]) as well as in atomic mass ( $m_C = 12.0$ ;  $m_{\text{Ti}} = 47.9$ ;  $m_W = 183.8$  amu [38]). Analogically, C is expected to be preferentially emitted along the surface normal and have longer mean free path than that of Ti and W.

To explain changes in the C content with varying the peak target current density (cf. Fig. 6), we performed ion mass and energy spectroscopy analyses. Fig. 7 shows the time-averaged mass/charge scans recorded during WC-HiPIMS/Ti-DCMS at (a)  $J_T = 0.32$  and (b)  $1.36$  A/cm $^2$ . Independent of the peak current density, in addition to the expected  $\text{C}^+$ ,  $\text{Ar}^+$ , and  $\text{W}^+$  ions from the WC-HiPIMS source,  $\text{Ti}^+$  and  $\text{Ti}^{2+}$  ions are also observed. Considering that the ionization degree of the sputtered flux in DCMS discharges is low, the observed  $\text{Ti}^+$  and  $\text{Ti}^{2+}$  ion fluxes must originate from the interaction between HiPIMS and DCMS

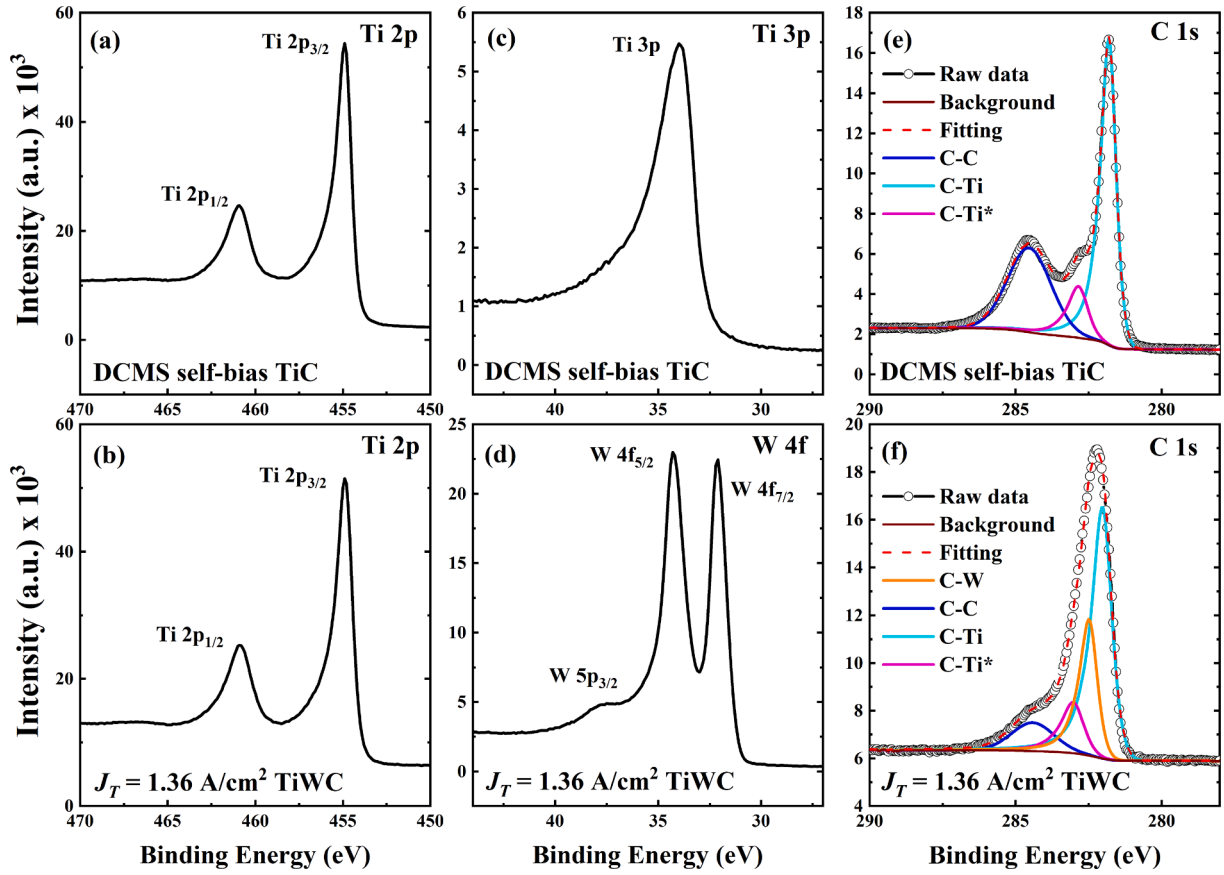


Fig. 5. XPS spectra of the DCMS self-bias TiC film: (a) Ti 2p, (c) Ti 3p, and (e) C 1s. Bottom row shows spectra from the WC-HiPIMS/TiC-DCMS TiWC film deposited with  $J_T = 1.36 \text{ A/cm}^2$  pulses (b) Ti 2p, (d) W 4f/Ti 3p, and (f) C 1s.

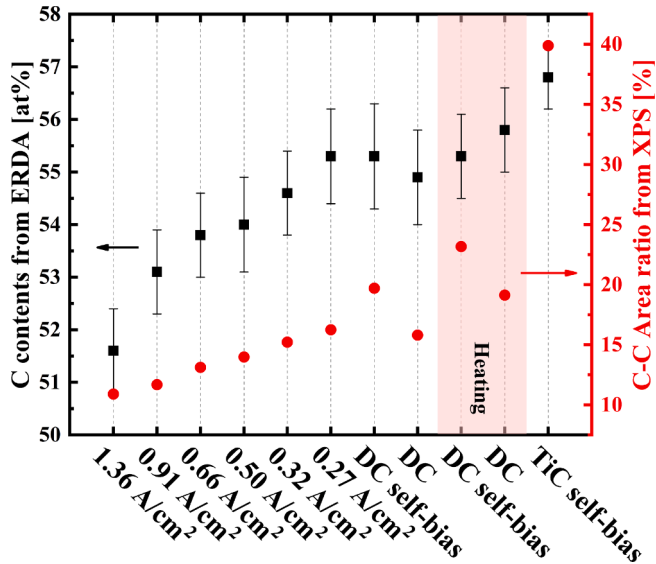


Fig. 6. Carbon elemental ratio from ERDA (left) and the C 1s signal fraction corresponding to the C—C peak (right) (All fitted results are presented in Fig. S5.).

plasmas. Due to the relatively low ionization potential of Ti ( $IP_{Ti}^1 = 6.8 \text{ eV}$  [38]), Ti neutrals can be ionized through electron impact ionization and charge transfer collisions while passing through denser plasma region of the HiPIMS plume [56,57]. The most notable change with increasing  $J_T$  is that the relative intensity between the  $W^{2+}$  and  $W^+$

fluxes increases. This is summarized in Fig. 7 (c) where the time- and energy-integrated ion flux ratios are plotted.

The profound change in the  $W^{2+}/W^+$  ratio, from 1.28 with  $J_T = 0.32 \text{ A/cm}^2$  to 6.07 with  $J_T = 1.36 \text{ A/cm}^2$ , implies the increasing role of the doubly-ionized W ions. This means that the mean energy of the heaviest energetic species bombarding the growing film surface increases with  $J_T$ , as the energy gained in the substrate sheath is twice higher for  $W^{2+}$  than it is for  $W^+$ . As a consequence, more profound preferential resputtering of lighter C atoms is expected with increasing  $J_T$ . Such resputtering has been reported for growth of other material systems including WC<sub>x</sub> [58], TiW [59], and TiC/a-C:H films [60]. Results shown in Fig. 7 (c) reveal that also the population of  $C^+$  ions increase with  $J_T$ . However,  $C^+$  ions constitute only a small fraction of the total C flux to the substrate due to higher ionization potential ( $IP_C^1 = 11.26 \text{ eV}$  vs  $IP_W^1 = 7.86$  [38]) and smaller electron impact cross-section [61,62]. Thus, we do not expect that the increase in  $C^+$  has a larger effect on film stoichiometry. Nevertheless, the results presented above demonstrate that the hybrid growth scenario provides an easy way to fine-tune the relative content of the a-C phase in TiWC films.

### 3.5. Film morphology

Scanning electron microscopy images of fractured cross sections and surface morphology of the studied films are presented in Fig. 8. The film thickness varies between 1.49 and 1.94  $\mu\text{m}$ , with most films being around 1.7  $\mu\text{m}$ . All the fractured cross sections display a columnar microstructure, which is in contrast to the featureless nanocomposite structures reported for nc-TiC/a-C(:H) [63]. Surface topography analysis shows narrow spacings between the grains, in the TiC and DCMS self-bias TiWC films, and most pronounced for films grown without heating and ion irradiation, which could be caused by the formation of a void

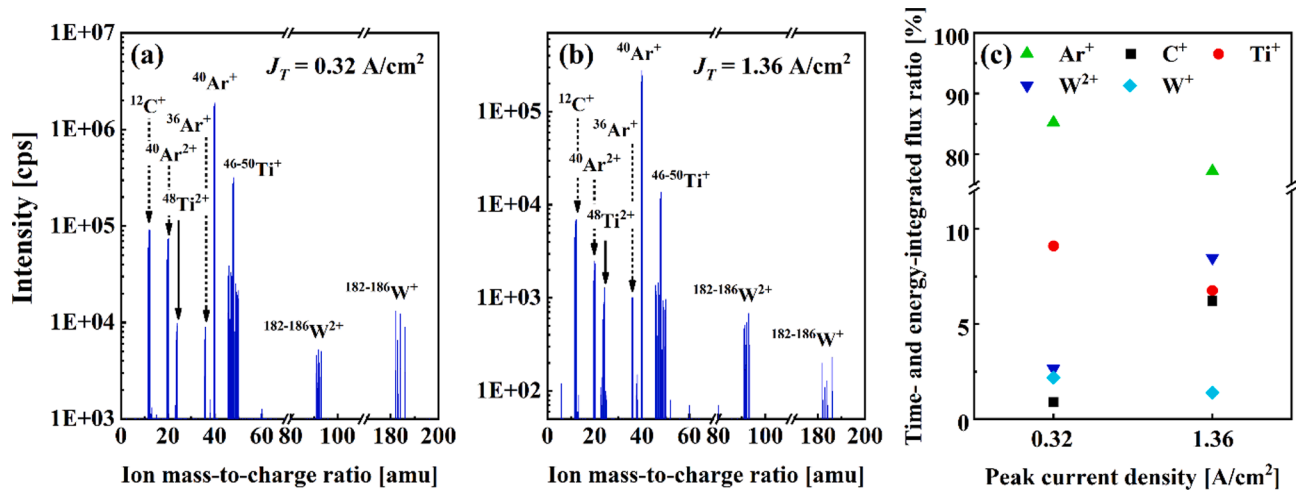


Fig. 7. Time-averaged ion mass-to-charge ratio scans at fixed energy by mass-energy-analyzer using hybrid configuration, where the peak current density ( $J_T$ ) varies from (a) 0.32 and (b) 1.36. The time- and energy-integrated ion flux ratio is presented in (c). The corresponding changes in DCMS power with different peak current densities can be found in Table 1.

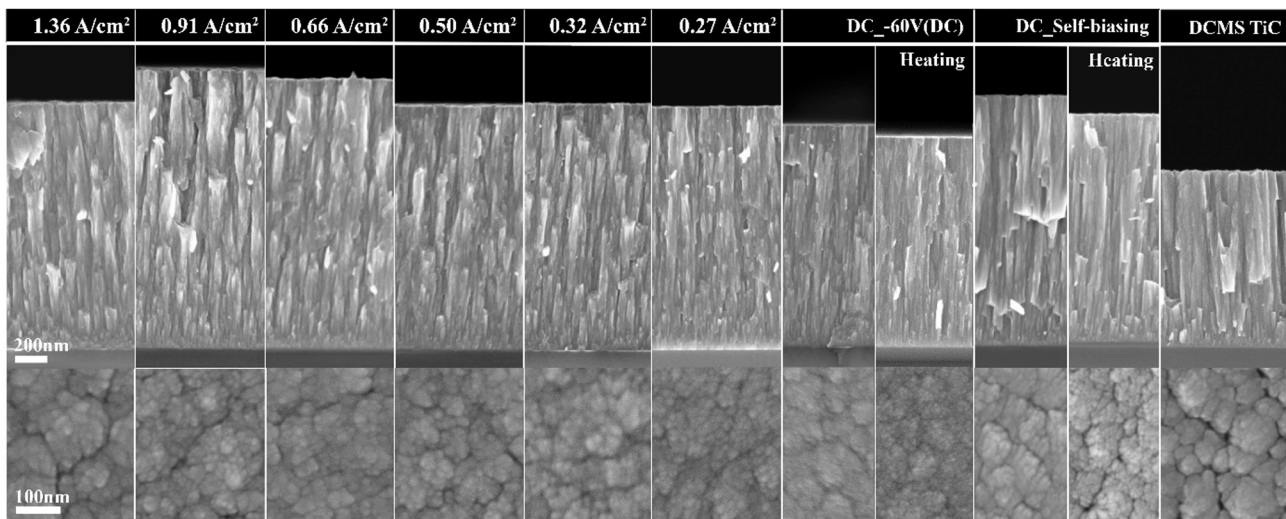


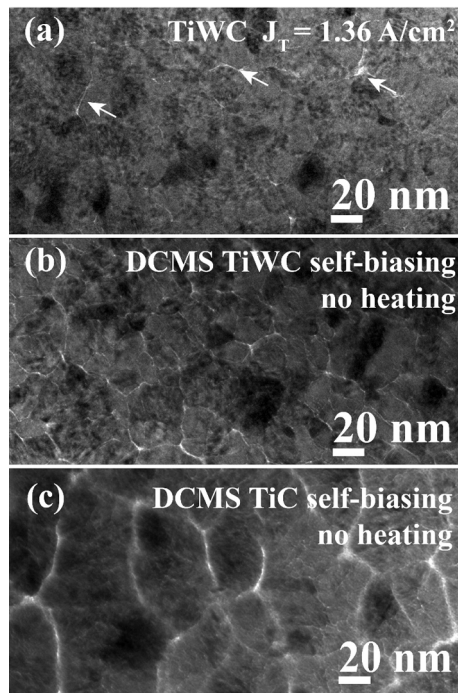
Fig. 8. Cross-sectional (upper row) and surface morphological (lower row) SEM images of TiWC samples grown by hybrid co-sputtering configuration with different  $J_T$  on HiPIMS source from 1.36 to 0.27  $\text{A/cm}^2$ , and samples grown by DCMS mode with and without external heating during the deposition process.

or the presence of a-C tissue layer. These features are less apparent in TiWC films deposited with  $-60 \text{ V}$ , however, are more apparent for the films with the highest  $J_T$  (i.e., higher  $\text{W}^+$  ion fluxes) of 1.36 and 0.91  $\text{A/cm}^2$ . To minimize the effect from topography and to better resolve the differences in the inter-grain structure, plan-view TEM images of selected samples are presented in Fig. 9. In Fig. 9 (a), the hybrid TiWC films grown with  $J_T = 1.36 \text{ A/cm}^2$  are denser than the DCMS self-bias samples (cf. Fig. 9 (b)), i.e., fewer intercolumnar pores or a-C tissue phases are observed. DCMS TiC grown with self-biasing and without external heating is less dense than TiWC films. This is seen as well-defined and wider bright lines separating the columns in Fig. 9 (c), which, based on the high oxygen content (cf. ERDA results in Fig. 3), are primarily ascribed to porosity. However, the presence of a-C phase in this area cannot be completely excluded. Oxygen incorporated in the films during growth is on the order of 0.5 at.%, anything above that level is due to the O adsorption during air exposure and, hence, can be used as the measure of film porosity [64]. The oxygen content is high,  $1.9 \leq [\text{O}] \leq 4.4 \text{ at\%}$ , in the self-bias TiWC films and low,  $0.5 \leq [\text{O}] \leq 0.9 \text{ at\%}$ , in the  $-60 \text{ V}$  bias ones, revealing a pronounced densification in the latter case.

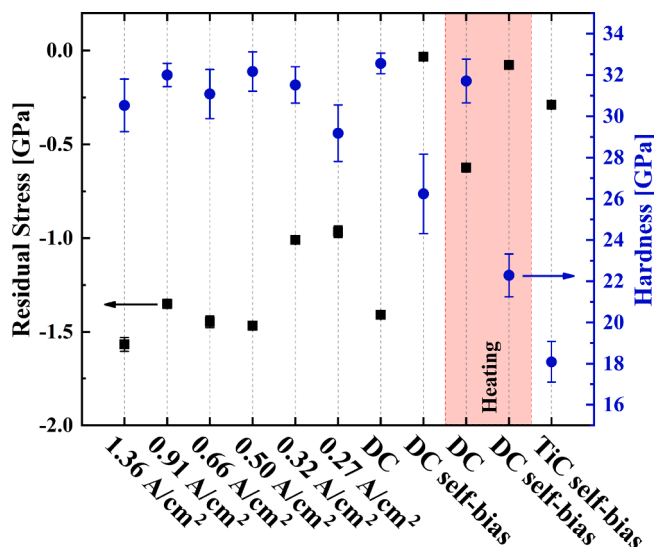
### 3.6. Mechanical properties

Fig. 10 shows the hardness and residual stress of all TiWC films. The TiC self-biased film is softest ( $H = 18.1 \pm 1.0 \text{ GPa}$ ). Once W is introduced, the hardness of the two DCMS TiWC self-biased films increase to  $H = 22.3 \pm 1.0$  and  $26.24 \pm 1.9 \text{ GPa}$  with and without external heating, respectively. The hardening mechanisms of these TiWC films can be inferred to be solid solution hardening due to the incorporation of W in c-TiC (c.f. Fig. 4). Alternatively, as suggested in Refs. [10,65], the more covalent bonding character in TiWC solid solutions may also account for hardening. The influence of W ion irradiation is determined by comparing the TiWC film grown by DCMS with floating substrates to the layer obtained by hybrid co-sputtering with  $J_T = 0.27 \text{ A/cm}^2$ . Although the current density is low, the hardness is  $H = 29.2 \pm 1.4 \text{ GPa}$ , which is harder than the self-bias films. The hardness increases further to approximately 32 GPa when the  $\text{W}^+$  ion irradiation increases ( $J_T \geq 0.32 \text{ A/cm}^2$ ). Such hardening can be a consequence of higher film density due to the fact that the ionization degree of sputtered W atoms increases with increasing peak target current density (c.f. Fig. 7). The effectiveness of  $\text{W}^+$  ion irradiation ( $J_T \geq 0.32 \text{ A/cm}^2$ ) for densification is manifested by





**Fig. 9.** Plan-view bright field TEM images of (a) TiWC grown by hybrid configuration with  $J_T = 1.36 \text{ A/cm}^2$ , (b) self-biasing TiWC grown in DCMS without external heating, and (c) self-biasing DCMS TiC without external heating. The white arrows indicate the less obvious intercolumnar features in (a).



**Fig. 10.** Residual stress (Left, square symbol) and hardness (Right, circle symbol) of the TiWC films grown in different deposition conditions (hybrid co-sputtering and DCMS).

the comparable hardness of TiWC films deposited by hybrid method and the layers deposited by DCMS with  $\text{Ar}^+$  ion irradiation and dc substrate bias. The additional hardening caused by  $\text{W}^+$  ion irradiation is likely an effect of a more effective introduction of interstitials and vacancies in the collision cascade.

Such defects result to residual stress in the films and all hybrid co-sputtered films have residual stresses in the range of  $-0.97 \leq \sigma \leq -1.57 \pm 0.04 \text{ GPa}$ . Films grown with high current densities ( $J_T \geq 0.5 \text{ A/cm}^2$ ) have higher compressive stresses,  $\sigma \approx -1.4 \text{ GPa}$ , compared to the

ones grown at lower current densities ( $0.27 \leq J_T \leq 0.36 \text{ A/cm}^2$ ),  $\sigma \approx -1.0 \text{ GPa}$ . The films grown without external biasing display a low residual stress ( $\sigma < -0.3 \text{ GPa}$ ).

### 3.7. Energy consumption

The potential to deposit dense and hard films at low processing temperatures by replacing the thermally driven adatom mobility with that provided by heavy ion irradiation has been discussed previously [22,25,64]. To demonstrate the differences of the energy consumption between the hybrid setup without external heating and DCMS self-bias with heating, we list out the energy differences to yield identical thicknesses of the TiWC sample by different deposition configuration in Table 2. The relative energy consumption per hour is reduced by 77 % with the hybrid co-sputtering setup, yet the WC-HiPIMS/TiC-DCMS film is harder than the self-biased film grown with external heating. Another benefit with low temperature growth is the wider selection of substrate that can be coated, for example temperature-sensitive materials such as polymers and metal alloys with specific microstructures.

## 4. Conclusions

$\text{Ti}_{1-x}\text{W}_x\text{C}$  ( $0.11 \leq x \leq 0.14$ ) films are deposited by non-reactive hybrid high-power impulse and dc magnetron co-sputtering (HiPIMS/DCMS) without external heating during deposition. Compound carbide targets,  $\text{W}_{0.5}\text{C}_{0.5}$  and  $\text{Ti}_{0.5}\text{C}_{0.5}$ , are operated under HiPIMS and DCMS conditions, respectively. The goal is to examine the effect of heavy metal-ion irradiation from the  $\text{W}_{0.5}\text{C}_{0.5}$  target on film nanostructure, composition, and density to minimize the contribution from working gas ions, a substrate bias with constant amplitude,  $-60 \text{ V}$ , is synchronized to the metal-ion rich time domain within each HiPIMS pulse. The intensity of W ion flux is controlled by altering the peak target current density ( $J_T$ ) from 0.27 to  $1.36 \text{ A/cm}^2$  through adjustment of the HiPIMS pulse length while keeping other parameters constant.

ERDA reveals that all layers are over stoichiometric in carbon. X-ray diffractometry  $\theta$ - $2\theta$  scan results show that all films form single metastable B1 structured TiWC. The transition from 111 to 200 preferred orientation is observed upon increasing the intensity of the  $\text{W}^+$  irradiation, which is explained by more effective resputtering of 111-oriented grains. In agreement with the C concentrations obtained from ERDA, X-ray photoelectron spectroscopy (XPS) results show that the fraction of amorphous C (i.e., the C—C contribution) decreases with increasing  $J_T$ . Using ion mass and energy spectroscopy analyses we observed the 5-fold increase in the  $\text{W}^{2+}/\text{W}^+$  ratio with increasing  $J_T$  from 0.32 to  $1.36 \text{ A/cm}^2$ , which allows to explain changes in the C/metal ratio by preferential resputtering of lighter C atoms. The relative content of the a-C phase in TiWC films can be, thus, easily tuned by varying  $J_T$  in the hybrid growth scenario. The effectiveness of the near surface intermixing due to the  $\text{W}^+$  ion irradiation is highlighted by comparing TiWC films deposited by the hybrid method with no substrate heating to layers grown by conventional DCMS technique with heating. The former film is dense and possesses high hardness ( $H \geq 31 \text{ GPa}$ ) while the energy consumption is reduced by at least 77 %.

### CRedit authorship contribution statement

**Tun-Wei Hsu:** Conceptualization, Investigation, Formal analysis, Data curation, Writing – original draft. **Grzegorz Greczynski:** Project administration, Conceptualization, Supervision, Formal analysis, Writing – review & editing. **Robert Boyd:** Formal analysis, Writing – review & editing. **Szilárd Kolozsvári:** Resources, Writing – review & editing. **Peter Polcik:** Resources, Writing – review & editing. **Magnus Odén:** Project administration, Conceptualization, Supervision, Funding acquisition, Writing – review & editing.



**Table 2**Energy consumption differences between hybrid co-sputtering (using  $J_T = 0.5 \text{ A/cm}^2$  as the example) and DCMS setup.

Deposition configuration	Baking	Deposition		Energy consumption per hour <sup>(a, b)</sup>	
	Heater	Heater	Total energies from target (TiC*2 + WC)	Substrate bias	
Hybrid	2 kW*2 (1 h) + 0 kW (1 h, cooling)	0	3.2 kW*2 + 0.5 kW (0.7 h)	0.014 kW (0.7 h)	4.4 kWh
DCMS	8.8 kW*2 (2 h)	8 kW*2 (0.5 h)	4.5 kW*2 + 0.22 kW (0.5 h)	0	19.1 kWh

(a) The energy consumption per hour was calculated by summing the power\*hours from each listed components and divided by the total deposition times of 2.7 h for hybrid and 2.5 h for DCMS. (b) Other energy consumption from the system, e.g., vacuum system, were similar and not considered for comparison.

## Declaration of Competing Interest

The authors declare that they have no known competing financial interests or personal relationships that could have appeared to influence the work reported in this paper.

## Data availability

Data will be made available on request.

## Acknowledgements

The authors acknowledge the financial support from VINNOVA (FunMat-II project grant no. 2016-05156), the Swedish Research Council (grants no 2017-03813 and 2017-06701), and the Swedish government strategic research area grant AFM – SFO MatLiU (2009-00971). The authors would like to thank Dr Babak Bakht for assistance with ToF-ERDA analysis, Dr Erik Lewin for suggestions on XPS data processing, and Dr Oleksandr Pshyk for acquiring WC reference XPS data.

## Appendix A. Supplementary data

Supplementary data to this article can be found online at <https://doi.org/10.1016/j.apsusc.2023.156639>.

## References

- [1] P.H. Mayrhofer, R. Rachbauer, D. Holec, F. Rovere, J. Schneider, Protective transition metal nitride coatings, *Comprehens. Mater. Proceed.* (2014) 355–388.
- [2] L. Toth, *Transition metal carbides and nitrides*, Elsevier, 2014.
- [3] P. Souček, J. Daniel, J. Hnilica, K. Bernátová, L. Zábranský, V. Buršíková, M. Stupavská, P. Vašina, Superhard nanocomposite nc-TiC/aC: H coatings: The effect of HiPIMS on coating microstructure and mechanical properties, *Surf. Coat. Technol.* 311 (2017) 257–267.
- [4] P. Souček, T. Schmidová, L. Zábranský, V. Buršíková, P. Vašina, O. Caha, J. Buršík, V. Peřina, R. Mikšová, Y. Pei, On the control of deposition process for enhanced mechanical properties of nc-TiC/aC: H coatings with DC magnetron sputtering at low or high ion flux, *Surf. Coat. Technol.* 255 (2014) 8–14.
- [5] N. Archer, The plasma-assisted chemical vapour deposition of TiC, TiN and TiC<sub>x</sub>N<sub>1-x</sub>, *Thin Solid Films* 80 (1981) 221–225.
- [6] R. Haubner, M. Lessiak, R. Pitonak, A. Köpf, R. Weissenbacher, Evolution of conventional hard coatings for its use on cutting tools, *Int. J. Refract. Metal Hard Mater.* 62 (2017) 210–218.
- [7] P. Fang, C. Mulligan, R. Jia, J. Shi, S. Khare, D. Gall, Epitaxial TiC<sub>x</sub> (001) layers: phase formation and physical properties vs C-to-Ti ratio, *Acta Mater.* 117643 (2022).
- [8] L. Karlsson, L. Hultman, M. Johansson, J.-E. Sundgren, H. Ljungcrantz, Growth, microstructure, and mechanical properties of arc evaporated TiC<sub>x</sub>N<sub>1-x</sub> (0 ≤ x ≤ 1) films, *Surf. Coat. Technol.* 126 (2000) 1–14.
- [9] H. Wang, S. Zhang, Y. Li, D. Sun, Bias effect on microstructure and mechanical properties of magnetron sputtered nanocrystalline titanium carbide thin films, *Thin Solid Films* 516 (2008) 5419–5423.
- [10] D. Edström, D. Sangiovanni, L. Hultman, I. Petrov, J.E. Greene, V. Chirita, Elastic properties and plastic deformation of TiC- and VC-based pseudobinary alloys, *Acta Mater.* 144 (2018) 376–385.
- [11] H.X. Ji, C.C. Amato-Wierda, Chemical vapor deposition of Ti□W□C thin films, *Surf. Coat. Technol.* 148 (2001) 262–267.
- [12] S.H. Koutzaki, J.E. Krzanowski, J.J. Nainaparampil, Phase formation and microstructure in sputter-deposited Ti-Mo-C and Ti-WC thin films, *Metall. Mater. Trans. A* 33 (2002) 1579–1588.
- [13] L. Rogström, M. Johansson, N. Ghafoor, L. Hultman, M. Odén, Influence of chemical composition and deposition conditions on microstructure evolution during annealing of arc evaporated ZrAlN thin films, *J. Vac. Sci. Technol. A* 30 (2012) 031504.
- [14] H. Oettel, R. Wiedemann, Residual stresses in PVD hard coatings, *Surf. Coat. Technol.* 76 (1995) 265–273.
- [15] I. Petrov, L. Hultman, J.E. Sundgren, J. Greene, Polycrystalline TiN films deposited by reactive bias magnetron sputtering: Effects of ion bombardment on resputtering rates, film composition, and microstructure, *J. Vac. Sci. Technol. A* 10 (1992) 265–272.
- [16] G. Greczynski, S. Mráz, J. Schneider, L. Hultman, Metal-ion subplantation: A game changer for controlling nanostructure and phase formation during film growth by physical vapor deposition, *J. Appl. Phys.* 127 (2020) 180901.
- [17] G. Greczynski, I. Zhirkov, I. Petrov, J.E. Greene, J. Rosen, Time evolution of ion fluxes incident at the substrate plane during reactive high-power impulse magnetron sputtering of groups IVb and Vb transition metals in Ar/N<sub>2</sub>, *J. Vac. Sci. Technol. A* 36 (2018) 020602.
- [18] K. Macák, V. Kouznetsov, J. Schneider, U. Helmersson, I. Petrov, Ionized sputter deposition using an extremely high plasma density pulsed magnetron discharge, *J. Vac. Sci. Technol. A* 18 (2000) 1533–1537.
- [19] G. Greczynski, J. Lu, J. Jensen, I. Petrov, J.E. Greene, S. Bolz, W. Kölker, C. Schiffrs, O. Lemmer, L. Hultman, Metal versus rare-gas ion irradiation during Ti1-xAlxN film growth by hybrid high power pulsed magnetron/dc magnetron co-sputtering using synchronized pulsed substrate bias, *J. Vac. Sci. Technol. A* 30 (2012) 061504.
- [20] G. Greczynski, I. Petrov, J.E. Greene, L. Hultman, Paradigm shift in thin-film growth by magnetron sputtering: from gas-ion to metal-ion irradiation of the growing film, *J. Vac. Sci. Technol. A* 37 (2019) 060801.
- [21] G. Greczynski, J. Lu, S. Bolz, W. Kölker, C. Schiffrs, O. Lemmer, I. Petrov, J. E. Greene, L. Hultman, Novel strategy for low-temperature, high-rate growth of dense, hard, and stress-free refractory ceramic thin films, *J. Vac. Sci. Technol. A* 32 (2014) 041515.
- [22] X. Li, B. Bakht, M.J. Jösaar, L. Hultman, I. Petrov, G. Greczynski, Toward energy-efficient physical vapor deposition: Routes for replacing substrate heating during magnetron sputter deposition by employing metal ion irradiation, *Surf. Coat. Technol.* 415 (2021) 127120.
- [23] H. Fager, O. Tengstrand, J. Lu, S. Bolz, B. Mesic, W. Kölker, C. Schiffrs, O. Lemmer, J.E. Greene, L. Hultman, Low-temperature growth of dense and hard Ti0.41Al0.51Ta0.08N films via hybrid HiPIMS/DC magnetron co-sputtering with synchronized metal-ion irradiation, *J. Appl. Phys.* 121 (2017) 171902.
- [24] Z. Wu, O. Tengstrand, B. Bakht, J. Lu, J.E. Greene, L. Hultman, I. Petrov, G. Greczynski, Growth of dense, hard yet low-stress Ti0.40Al0.27W0.33N nanocomposite films with rotating substrate and no external substrate heating, *J. Vacuum Sci. Technol. A: Vacuum, Surf., Films*, 38 (2020) 023006.
- [25] X. Li, B. Bakht, M.J. Jösaar, I. Petrov, L. Hultman, G. Greczynski, Towards energy-efficient physical vapor deposition: Mapping out the effects of W+ energy and concentration on the densification of TiAlWN thin films grown with no external heating, *Surf. Coat. Technol.* 424 (2021) 127639.
- [26] H. Schobert, Production of acetylene and acetylene-based chemicals from coal, *Chem. Rev.* 114 (2014) 1743–1760.
- [27] B. Bakht, I. Petrov, J.E. Greene, L. Hultman, J. Rosén, G. Greczynski, Controlling the B/Ti ratio of TiB<sub>x</sub> thin films grown by high-power impulse magnetron sputtering, *J. Vac. Sci. Technol. A* 36 (2018) 030604.
- [28] D. Lundin, M. Čada, Z. Hubička, Ionization of sputtered Ti, Al, and C coupled with plasma characterization in HiPIMS, *Plasma Sources Sci. Technol.* 24 (2015) 035018.
- [29] P. Zaumseil, High-resolution characterization of the forbidden Si 200 and Si 222 reflections, *J. Appl. Cryst.* 48 (2015) 528–532.
- [30] J. Keckes, E. Eiper, K. Martinschitz, H. Köstenbauer, R. Daniel, C. Mitterer, High-temperature residual stresses in thin films characterized by x-ray diffraction substrate curvature method, *Rev. Sci. Instrum.* 78 (2007) 036103.
- [31] G.C. Janssen, M. Abdalla, F. Van Keulen, B. Pujada, B. Van Venrooy, Celebrating the 100th anniversary of the Stoney equation for film stress: Developments from polycrystalline steel strips to single crystal silicon wafers, *Thin Solid Films* 517 (2009) 1858–1867.
- [32] L.B. Freund, S. Suresh, *Thin film materials: stress, defect formation and surface evolution*, Cambridge university press 2004.
- [33] G. Greczynski, D. Primetzhofer, L. Hultman, Reference binding energies of transition metal carbides by core-level x-ray photoelectron spectroscopy free from Ar+ etching artefacts, *Appl. Surf. Sci.* 436 (2018) 102–110.

- [34] G. Greczynski, L. Hultman, Reliable determination of chemical state in x-ray photoelectron spectroscopy based on sample-work-function referencing to adventitious carbon: resolving the myth of apparent constant binding energy of the C 1s peak, *Appl. Surf. Sci.* 451 (2018) 99–103.
- [35] N.X.r.P.S. Database, NIST Standard Reference Database Number 20, National Institute of Standards and Technology, Gaithersburg MD, 20899, (2000).
- [36] J. Bohlmark, M. Lattemann, J. Gudmundsson, A. Ehasarian, Y.A. Gonzalvo, N. Brenning, U. Helmersson, The ion energy distributions and ion flux composition from a high power impulse magnetron sputtering discharge, *Thin Solid Films* 515 (2006) 1522–1526.
- [37] I. Zhirkov, A. Eriksson, A. Petruhins, M. Dahlqvist, A.S. Ingason, J. Rosén, Effect of Ti-Al cathode composition on plasma generation and plasma transport in direct current vacuum arc, *J. Appl. Phys.* 115 (2014) 123301.
- [38] W.M. Haynes, *CRC handbook of chemistry and physics*, CRC press 2014.
- [39] J.C. Oliveira, F. Ferreira, A. Anders, A. Cavaleiro, Reduced atomic shadowing in HiPIMS: Role of the thermalized metal ions, *Appl. Surf. Sci.* 433 (2018) 934–944.
- [40] W.C. Oliver, G.M. Pharr, An improved technique for determining hardness and elastic modulus using load and displacement sensing indentation experiments, *J. Mater. Res.* 7 (1992) 1564–1583.
- [41] M. Morris, H. McMurdie, E. Evans, B. Paretkin, H. Parker, N. Panagiotopoulos, C. Hubbard, Standard X-ray diffraction powder patterns, National Bureau of Standards monograph 25 section 18 (Library of congress catalog card number: 53–61386), National Bureau of Standards, 1981.
- [42] G. Greczynski, J. Lu, M. Johansson, J. Jensen, I. Petrov, J.E. Greene, L. Hultman, Role of  $Ti^{n+}$  and  $Al^{n+}$  ion irradiation ( $n=1, 2$ ) during  $Ti_{1-x}Al_xN$  alloy film growth in a hybrid HiPIMS/magnetron mode, *Surf. Coat. Technol.* 206 (2012) 4202–4211.
- [43] J. Greene, J.E. Sundgren, L. Hultman, I. Petrov, D. Bergstrom, Development of preferred orientation in polycrystalline TiN layers grown by ultrahigh vacuum reactive magnetron sputtering, *Appl. Phys. Lett.* 67 (1995) 2928–2930.
- [44] D. Zhou, S. Jin, Y. Li, F. Qiu, F. Deng, J. Wang, Q. Jiang, Effect of stoichiometry on the surface energies of 100 and 111 and the crystal shape of TiC x and TiN x, *CrstEngComm* 15 (2013) 643–649.
- [45] L. Hultman, J.E. Sundgren, J. Greene, D. Bergstrom, I. Petrov, High-flux low-energy ( $\approx 20$  eV)  $N^+$  2 ion irradiation during TiN deposition by reactive magnetron sputtering: Effects on microstructure and preferred orientation, *J. Appl. Phys.* 78 (1995) 5395–5403.
- [46] D. Briggs, *Surface analysis of polymers by XPS and static SIMS*, Cambridge University Press, 1998.
- [47] E. Lewin, P.Å. Persson, M. Lattemann, M. Stüber, M. Gorgoi, A. Sandell, C. Ziebert, F. Schäfers, W. Braun, J. Halbritter, On the origin of a third spectral component of C1s XPS-spectra for nc-TiC/aC nanocomposite thin films, *Surf. Coat. Technol.* 202 (2008) 3563–3570.
- [48] A.V. Naumkin, A. Kraut-Vass, S.W. Gaarenstroom, C.J. Powell, NIST X-ray photoelectron spectroscopy database 10 (2012) T4T88K. NIST standard reference database 20, version 4.1.,
- [49] E. Lewin, M. Gorgoi, F. Schäfers, S. Svensson, U. Jansson, Influence of sputter damage on the XPS analysis of metastable nanocomposite coatings, *Surf. Coat. Technol.* 204 (2009) 455–462.
- [50] G. Greczynski, L. Hultman, X-ray photoelectron spectroscopy: towards reliable binding energy referencing, *Prog. Mater. Sci.* 107 (2020) 100591.
- [51] P. Eklund, J. Emmerlich, H. Högberg, O. Wilhelmsson, P. Isberg, J. Birch, P. Å. Persson, U. Jansson, L. Hultman, Structural, electrical, and mechanical properties of nc-Ti C/ a-Si C nanocomposite thin films, *J. Vacuum Sci. Technol. B: Microelectron. Nanometer Struct. Process., Measur., Phenomena* 23 (2005) 2486–2495.
- [52] P. Eklund, M. Beckers, J. Frodelius, H. Högberg, L. Hultman, Magnetron sputtering of Ti 3 Si C 2 thin films from a compound target, *J. Vac. Sci. Technol. A* 25 (2007) 1381–1388.
- [53] J. Frodelius, P. Eklund, M. Beckers, P.Å. Persson, H. Högberg, L. Hultman, Sputter deposition from a Ti2AlC target: Process characterization and conditions for growth of Ti2AlC, *Thin Solid Films* 518 (2010) 1621–1626.
- [54] J. Neidhardt, S. Mráz, J.M. Schneider, E. Strub, W. Böhne, B. Liedke, W. Möller, C. Mitterer, Experiment and simulation of the compositional evolution of Ti–B thin films deposited by sputtering of a compound target, *J. Appl. Phys.* 104 (2008) 063304.
- [55] E. Clementi, D. Raimondi, W.P. Reinhardt, Atomic screening constants from SCF functions. II. Atoms with 37 to 86 electrons, *J. Chem. Phys.* 47 (1967) 1300–1307.
- [56] M. Raadu, I. Axnäs, J.T. Gudmundsson, C. Huo, N. Brenning, An ionization region model for high-power impulse magnetron sputtering discharges, *Plasma Sources Sci. Technol.* 20 (2011) 065007.
- [57] J. Gudmundsson, Ionization mechanism in the high power impulse magnetron sputtering (HiPIMS) discharge, *Journal of Physics: Conference Series*, IOP Publishing, 2008, pp. 082013.
- [58] T. Glechner, C. Tomastik, E. Badisch, P. Polcik, H. Riedl, Influence of WC/C target composition and bias potential on the structure-mechanical properties of non-reactively sputtered WC coatings, *Surf. Coat. Technol.* 432 (2022) 128036.
- [59] L. Shaginyan, M. Mišina, S. Kadlec, L. Jastrabík, A. Mackova, V. Peřina, Mechanism of the film composition formation during magnetron sputtering of WTi, *J. Vac. Sci. Technol. A* 19 (2001) 2554–2566.
- [60] K. Shaha, Y. Pei, D. Martinez-Martinez, J. Sanchez-Lopez, J.T.M. De Hosson, Effect of process parameters on mechanical and tribological performance of pulsed-DC sputtered TiC/aC: H nanocomposite films, *Surf. Coat. Technol.* 205 (2010) 2633–2642.
- [61] K. Sarakinos, A. Braun, C. Zilkens, S. Mráz, J. Schneider, H. Zoubos, P. Patsalas, Exploring the potential of high power impulse magnetron sputtering for growth of diamond-like carbon films, *Surf. Coat. Technol.* 206 (2012) 2706–2710.
- [62] A. Ajaz, K. Sarakinos, D. Lundin, N. Brenning, U. Helmersson, A strategy for increased carbon ionization in magnetron sputtering discharges, *Diam. Relat. Mater.* 23 (2012) 1–4.
- [63] Y. Pei, D. Galvan, J.T.M. De Hosson, Nanostructure and properties of TiC/aC: H composite coatings, *Acta Mater.* 53 (2005) 4505–4521.
- [64] X. Li, B. Bakhit, M. Johansson Jösaar, I. Petrov, L. Hultman, G. Greczynski, Dense, single-phase, hard, and stress-free TiO. 32AlO. 63WO. 05N films grown by magnetron sputtering with dramatically reduced energy consumption, *Sci. Reports*, 12 (2022) 1–10.
- [65] B. Wang, Y. Liu, Y. Liu, J.-W. Ye, Mechanical properties and electronic structure of TiC, TiO. 75WO. 25C, TiO. 75WO. 25CO. 75NO. 25, TiCO. 75NO. 25 and TiN, *Physica B: Condensed Matter*, 407 (2012) 2542–2548.